Supporting Information

Fermi Level Alignment by Copper Doping for Efficient ITO/Perovskite Junction Solar Cells

Kai Lu[1,2#], Yan Lei[1#], Ruijuan Qi[3#], Jiang Liu[4], Xiaogang Yang[1]*, Zuxiao Jia[1],

Rui Liu[5], Yong Xiang[2], Zhi Zheng[1]*

[1]Key Laboratory for Micro-Nano Energy Storage and Conversion Materials of Henan Province, College of Advanced Materials and Energy, Institute of Surface Micro and Nano Materials, Xuchang University, Henan 461000, China.

[2]School of Energy Science and Engineering, University of Electronic Science and Technology of China, Chengdu 611731, China.

[3]Key Laboratory of Polar Materials and Devices, Ministry of Education, Department of Electronic Engineering, East China Normal University, Shanghai 200241, China

[4]Chengdu Green Energy and Green Manufacturing R&D Center, Chengdu Development Center of Science and Technology, China Academy of Engineering Physics, Chengdu, 610207, China.

[5]Joint Center for Artificial Photosynthesis, California Institute of Technology, Division of Chemistry and Chemical Engineering, Pasadena, CA 91125, United States

[#] These authors contributed equally.

*Corresponding Author email: xiaogang.yang@gmail.com (X.Y.) and zzheng@xcu.edu.cn (Z. Z.)

Figure S1

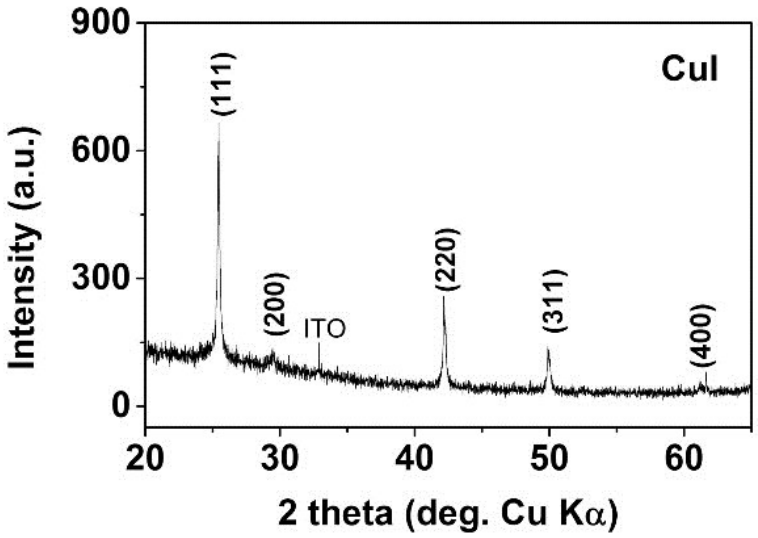

Figure S1. CuI (~103 nm) after the Cu film reacting with I_2 atmosphere on ITO substrate. The pattern is in good agreement with the cubic copper iodide in JCPDS card (No. 75-0831).

Figure S2

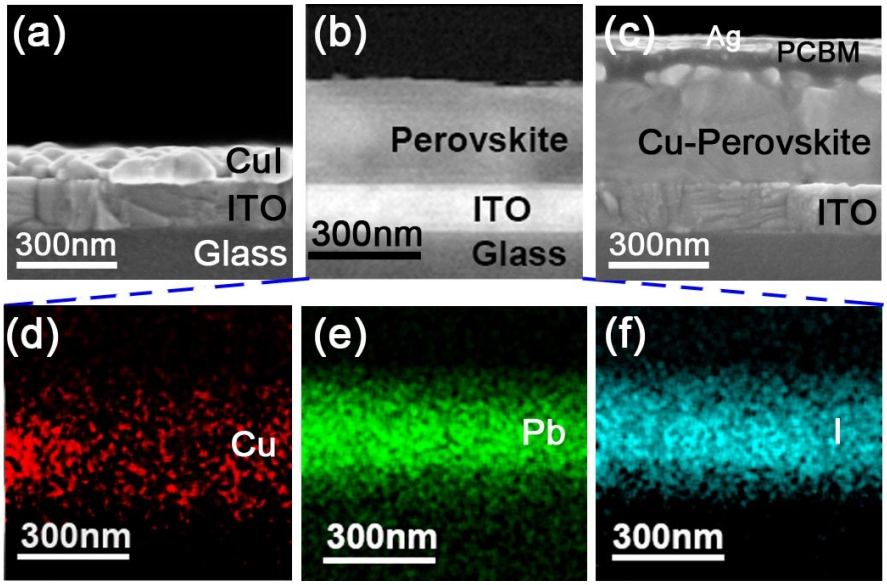

Figure S2. Cross-section FESEM images: a) ITO/CuI film; b) ITO/Cu20-perovskite film; c) assembled inverted ITO/$(CH_3NH_3)_{1-x}Cu_xPbI_3$/PCBM/Ag device; d-f) EDS elemental maps of Cu, Pb and I obtained at cross-section of ITO/Cu-perovskite. Figure S2a is the SEM image of the ITO/CuI cross-section converted from 20 nm elemental Cu, where the thickness of CuI layer about 103 nm. The resolution of Figure S2b is lower for the larger working distance during EDS mapping. The EDS mapping of Cu (d) showed the Cu vertically distributed from bottom to the top surface, which had lower uniformity due to the Cu concentration, sample thickness and instrument resolution.

Figure S3

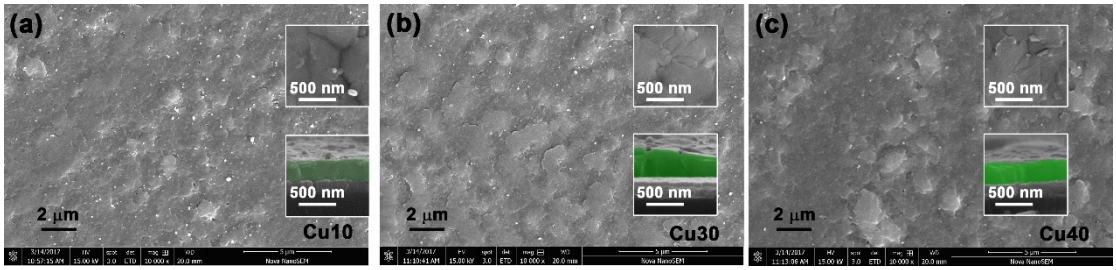

Figure S3. SEM images of the top surface of the Cu-perovskite films with CuI underlayer: (a) Cu10-perovskite; (b) Cu30-perovskite; (c) Cu40-perovskite. Higher resolution image and cross-section image are inserted on the top-right and middle-right, respectively. From the SEM images of the Cu doped perovskite films, we could find all the surfaces are conformal on the substrate. This high quality of the films can reduce the short circuit of the device in nanoscale. Moreover, the performance variation under different Cu doping level was less likely due to the film quality.

Figure S4

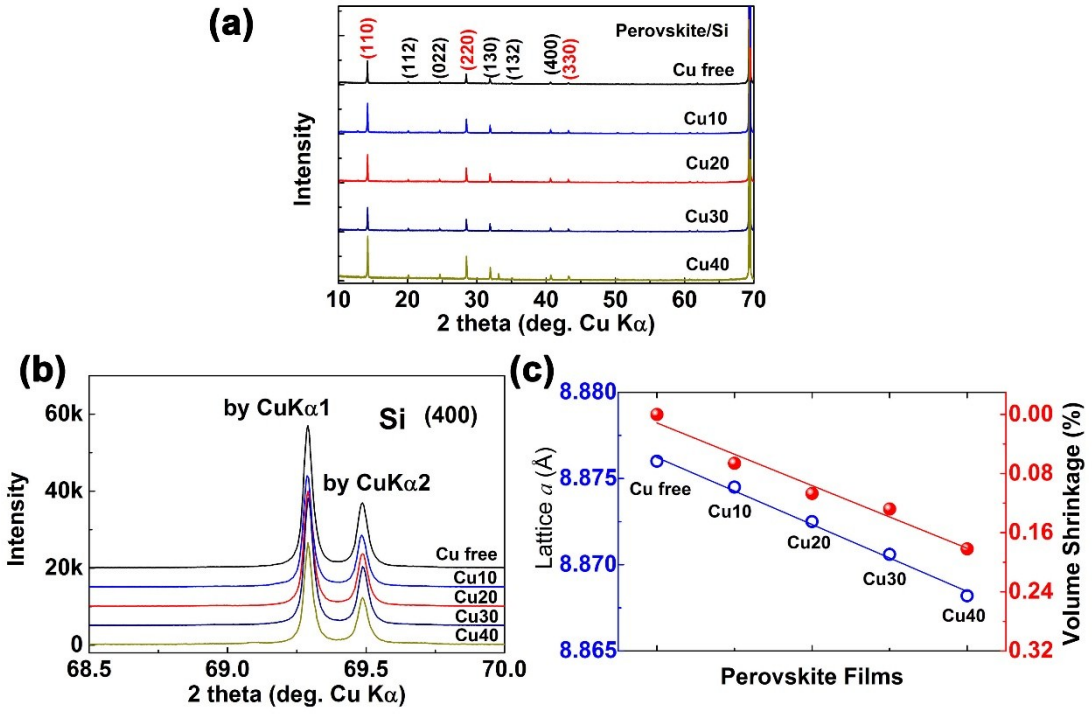

Figure S4. XRD pattern of perovskite on Si (200) wafer for lattice measurements: (a) full pattern, (b) Si(400) peaks. Cu10, Cu20, Cu30 and Cu40 corresponding to the various doping level of Cu in the perovskite films. XRD of Perovskite on Si wafer: Si(400) was set to 69.29°, corresponding to the card (JCPDS. No. 72.2108). (c) the parameter *a* and volume shrinkage based on the Si/perovskite.

Table S1

Table S1. The Lattice parameters of Cu doped and undoped perovskite on Si(400), calculated by using a Cell software (Copyright © 1986 by K. Dwight) and $CuK_{\alpha 1}$ (λ=1.5406 Å).

Perovskites	*a* (Å)	*c* (Å)	RMS errors	V (Å^3)	Δ V (%)
Cu free	8.8760	12.4899	1.10E-04	984.00	0.000
Cu10	8.8745	12.4859	1.20E-04	983.35	-0.066
Cu20	8.8725	12.4864	1.30E-04	982.95	-0.107
Cu30	8.8706	12.4892	1.40E-04	982.74	-0.128
Cu40	8.8682	12.4891	1.50E-04	982.20	-0.182

XRD showed the slight lattice shrinkage, due to the Cu^+ occupying the large size of $CH_3NH_3^+$, which is quite different from the other reports as the interstitial defects or partial substitution of Cu at Pb sites.[1] Although this lattice parameters are obtained on the perovskite deposited on Si substrate, we assumed the crystal quality and orientation were the same as those on ITO substrate. This lattice shrinkage suggested that the CuI acted as dopant rather than composites or blend in the perovskite matrix.

Figure S5

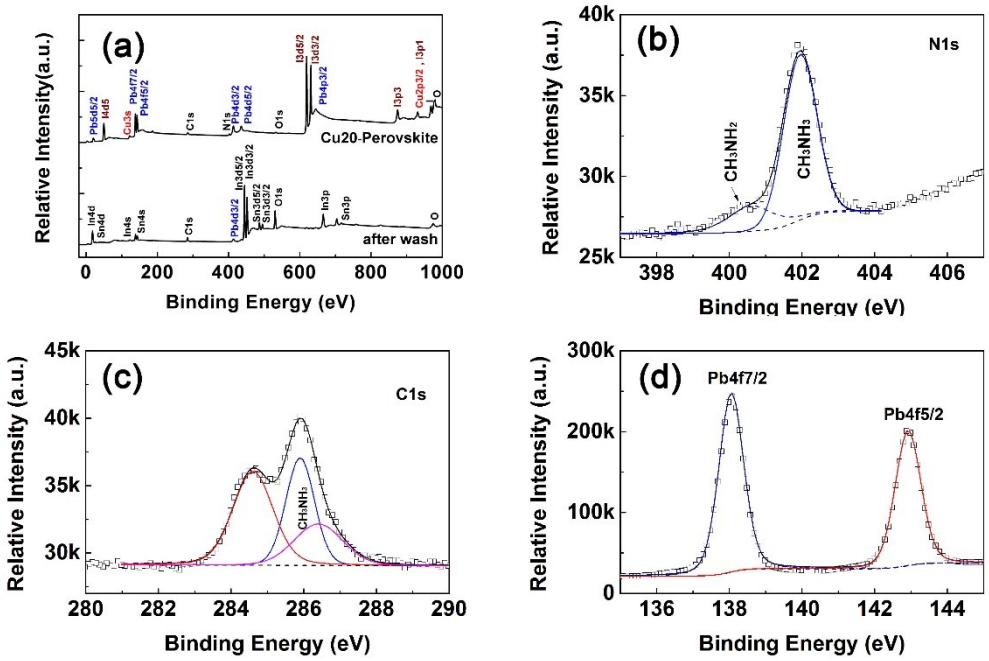

Figure S5. XPS spectra of the Cu-perovskite films: a) XPS survey spectra of Cu20-perovskite (upper line) and ITO interface after the removal of Cu20-perovskite by DMF; b) N1s; c) C1s and d) Pb4f. Based on the peak fitting as in Figure S4 and Cu2p in Figure 2f, the elements ratios were calculated according to the peak area and their sensitive factors. In Figure S5a, the N1s showed a shoulder peak close to 401 eV, which is attributed to the formation of CH_3NH_2 from CH_3NH_3.[2, 3] The I/Pb =2.5 is due to the deficiency of I elements, which is coincided with the literature reports.[4-6]

Figure S6.

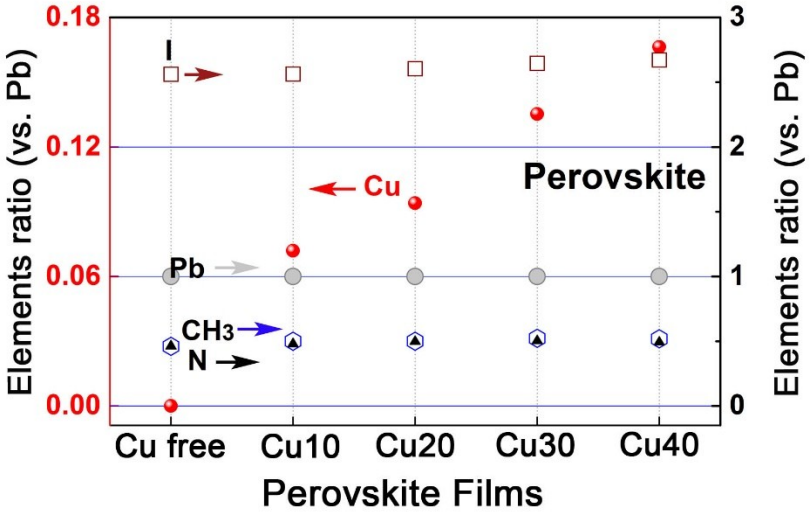

Figure S6. Elemental composition (vs. Pb) of the undoped and Cu-doped perovskite films through XPS.

Figure S7.

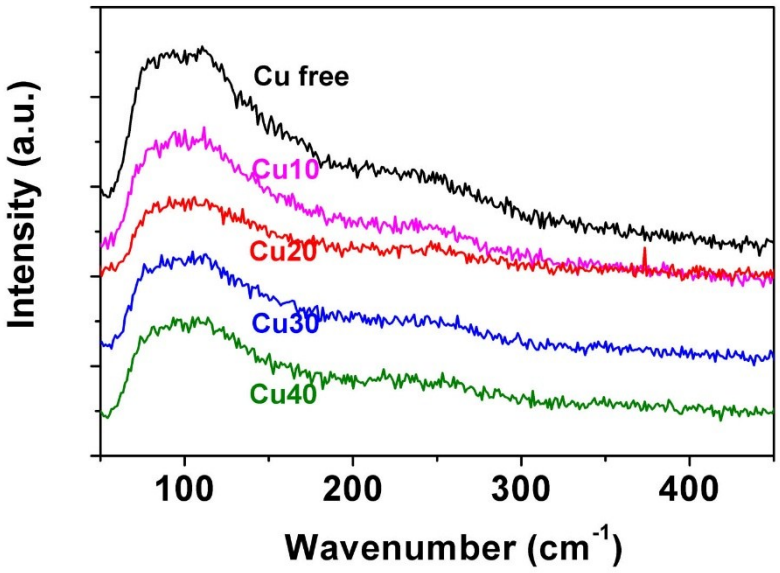

Figure S7. Raman spectra of the pure and Cu doped perovskite films. No peaks due to PbI_2 or CuI could be found. It was noting that the Raman spectra collection should be carried out at extremely low laser intensity. Otherwise, the perovskite films would be sintered by the laser irradiation, or convert to PbI_2 impurities. The spectra also suggested no PbI_2 impurities were detected from the fresh prepared perovskite.

Figure S8.

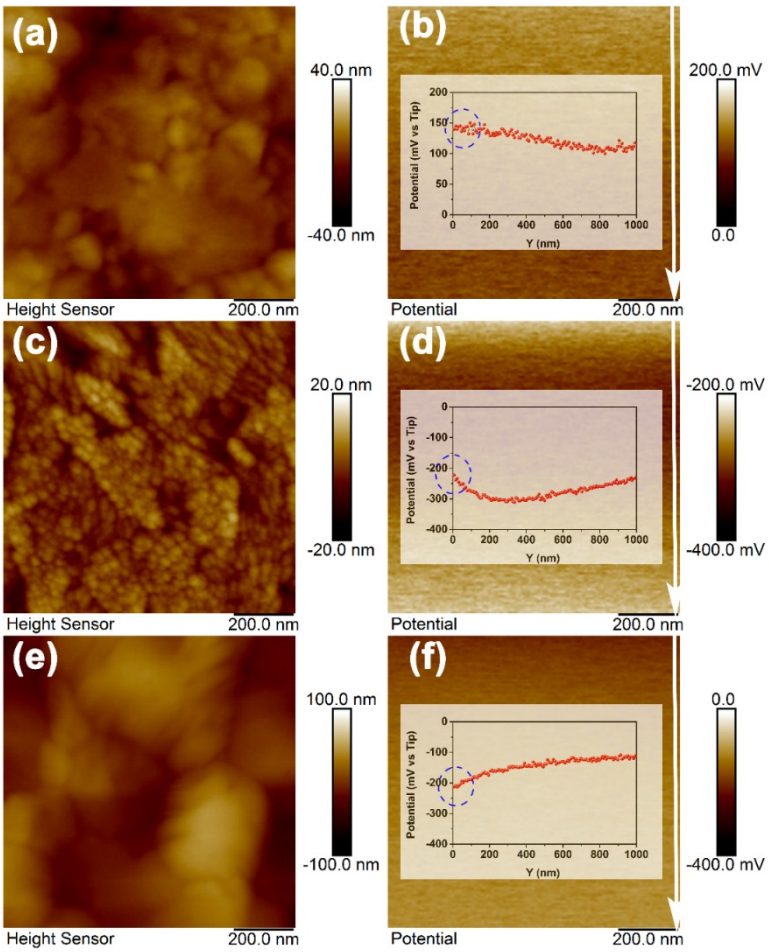

Figure S8. (a) Height image and (b) KPFM image of the Cu-free perovskite film on glass substrate; (c) height image and (d) KPFM image of the ITO substrate; (e) height image and (f) KPFM image of the Cu20-perovskite film on glass substrate. Inserted images were the Potential-Y section on the corresponded films. The potentials were measured versus Pt/Ir AFM tip. Blue cycles in the V~Y figures indicated the scanning starting point from top to bottom.

Figure S9.

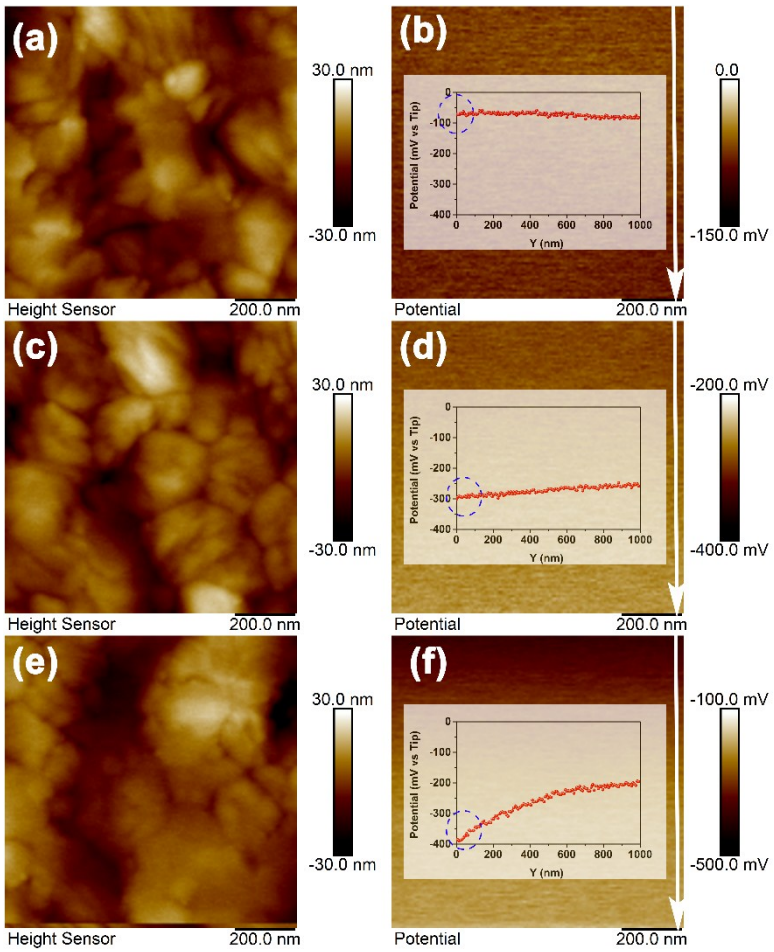

Figure S9. (a) Height image and (b) KPFM image of the Cu10-perovskite film on glass substrate; (c) height image and (d) KPFM image of the Cu30-perovskite film on glass substrate; (e) height image and (f) KPFM image of the Cu40-perovskite film on glass substrate. Inserted were the Potential-Y section on the corresponded films. The potentials were measured versus Pt/Ir AFM tip. Blue cycles in the V~Y figures indicated the scanning starting point from top to bottom.

Table S2. The CPDs of Cu-free perovskite and Cu doped perovskite from KPFM via the AFM tip.

Perovskite	Cu free	Cu10	Cu20	Cu30	Cu40	ITO
CPD (V)[a]	0.14	-0.07	-0.21	-0.30	-0.39	-0.22
Fermi Level (eV)	-5.44	-5.23	-5.09	-5.0	-4.91	-5.08

[a] The CPD values were calculated by using the equation of $\mathrm{CPD} = \phi_{\mathrm{tip}} - \phi_{\mathrm{sample}} = E_{\mathrm{sample}} - E_{\mathrm{tip}}$. Due to the air sensitive surface, the value was taken from the starting point of potential scanning (<3 min out from glove box).

Figure S10.

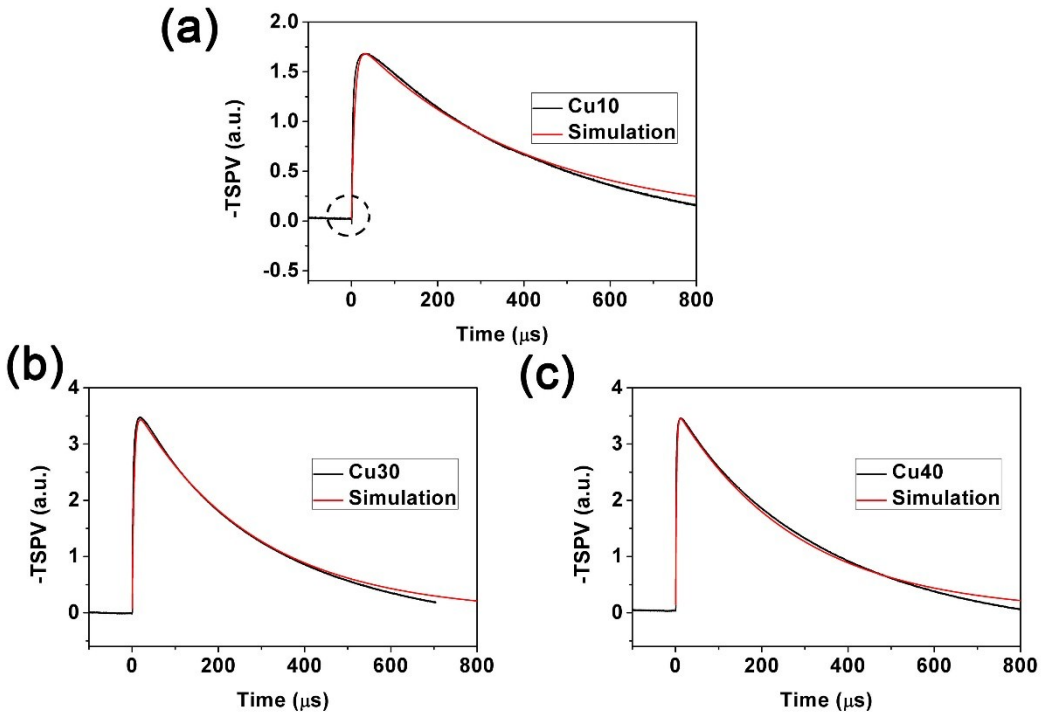

Figure S10. Experimental and simulated TSPV curves of the ITO/perovskite thin films with various Cu content: (a) Cu10; (b) Cu30 and (c) Cu40. Black dashed circle in (a) showing the slight negative signal due to the misalignment of the band structures of Cu10-perovskite and ITO substrate. It was found the simulated curves agreed well with the experiment curves in the spectra.

We speculated that the first order kinetic processes in the TSPV curves. Firstly, the surface charges density Q is proportional to the transient surface potential (V) detected at the surface, obeying the parallel plate capacitor property ($Q = C \cdot V$, where C is the capacitance for the TSPV setup).[7] Secondly, the charge separation is mainly due to the collection of photon-excited charges separated from the bulk of the perovskite film, where the separation rate is proportional to the excited charges in bulk ($k_{sep} \cdot Q_{exc}$). Thirdly, after the TSPV reached to a minimum (negative peak), the charge separation rate is comparable and the charge recombination rate is proportional to the charge absorbed at the solid/air surface, where it is much slower than the other bulk recombination modes. According to this charge separation and recombination assumption, we can write a consecutive reaction (Eq. 1) for the charge evolution (or TSPV) in the semiconductor:

$$Q_{exc} \xrightarrow{k_{sep}} Q_{sep} \xrightarrow{k_{rec}} Q_{rec} \qquad (1)$$

where Q_{exc}, Q_{sep} and Q_{rec} corresponded to the excited charges in the bulk semiconductor, the separated charges detected by TSPV, and the surface recombined charge, respectively. k_{sep} and k_{rec} are the rate constants for the charge separation and recombination, respectively. Obviously, only the separated charge Q_{sep} contributes to the TSPV signal, while the Q_{exc} and Q_{rec} don't. For the boundary condition (t=0, $Q_{sep,0}$=0, and $k_{rec} \neq k_{sep}$), the separated charges can be expressed as Eq. (2):[8]

$$Q_{sep} = \frac{k_{sep} Q_{exc,0}}{k_{rec} - k_{sep}} \left(e^{-k_{sep} t} - e^{-k_{rec} t} \right) \qquad (2)$$

Therefore, the transient surface photovoltage V can be written as Eq. (3):

$$V = -\frac{k_{sep} Q_{exc,0}}{\left(k_{rec} - k_{sep} \right) C} \left(e^{-k_{sep} t} - e^{-k_{rec} t} \right) \qquad (3)$$

Table S3. Kinetics parameters of the Cu-free and Cu doped ITO/Perovskite junctions through TSPV.

Perovskite	Cu free	Cu10	Cu20	Cu30	Cu40
T_{max} (s)	7.16×10^{-5}	3.15×10^{-5}	2.32×10^{-5}	1.93×10^{-5}	1.17×10^{-5}
k_{sep} (s^{-1})	5.42×10^{4}	1.24×10^{5}	1.80×10^{5}	2.15×10^{5}	4.11×10^{5}
k_{rec} (s^{-1})	1.22×10^{3}	2.52×10^{3}	2.95×10^{3}	3.60×10^{3}	3.52×10^{3}
$Q_{exc,0}$ (a.u.)[a]	0.45	1.82	2.12	3.68	3.60

[a]: the relative value of the $Q_{exc,0}$ were shown here.

Figure S11

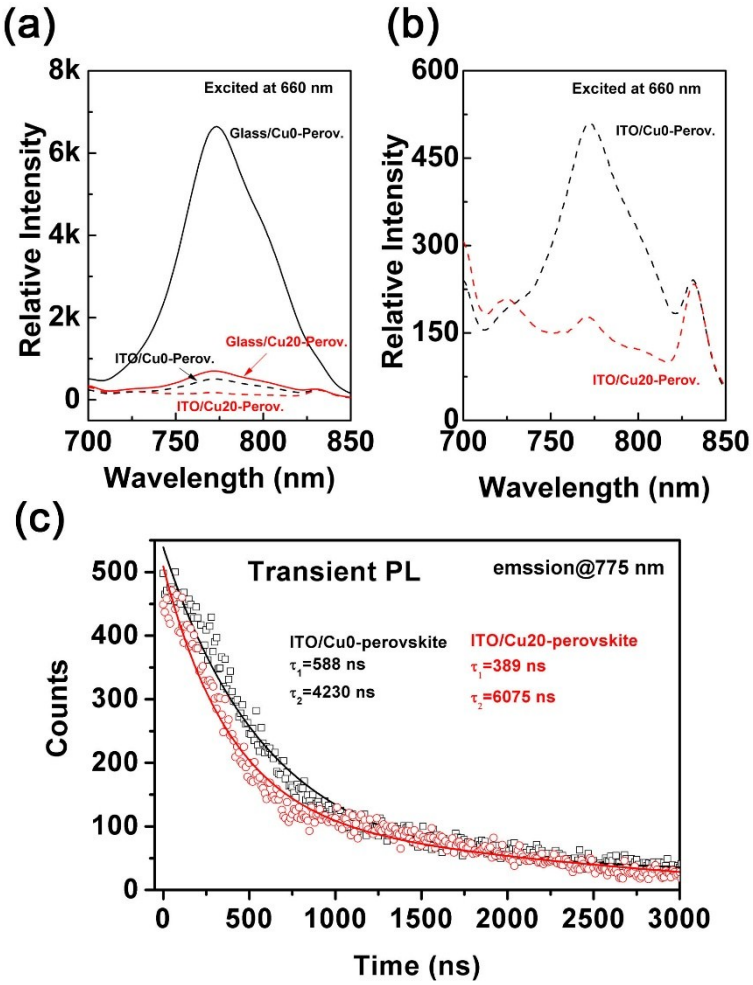

Figure S11. Photoluminescence of the undoped and Cu20 doped perovskite films excited at 660 nm: a) PL emission peaks of glass/Cu0-perovskite (black solid line), glass/Cu20-perovskite (red solid line), ITO/Cu0-perovskite (black dashed line) and ITO/Cu20-perovskite (red dashed line); b) zoomed in image of PL curves of the ITO/Cu0-perovskite (black dashed line) and ITO/Cu20-perovskite (red dashed line); c) normalized time-resolved PL transient decay of the ITO/Cu0-perovskite (black square) and ITO/Cu20-perovskite (red circle), the emission measured at 775 nm. The simulation was based on double exponential components decay.

The PL intensity of the perovskite on ITO was much lower than that on glass due to the easier charge transferred to ITO. When Cu introduced into the perovskite films, the PL intensity was further suppressed due to the better charge separation and collection at the ITO electrode. Transient PL showed double exponential decay on the samples: for shorter lifetime (τ_1) the ITO/Cu20-perovskite showed slight shorter than the ITO/perovskite sample due to the charge separation; while the longer lifetime (τ_2) may ascribed to surface trap states.

Figure S12

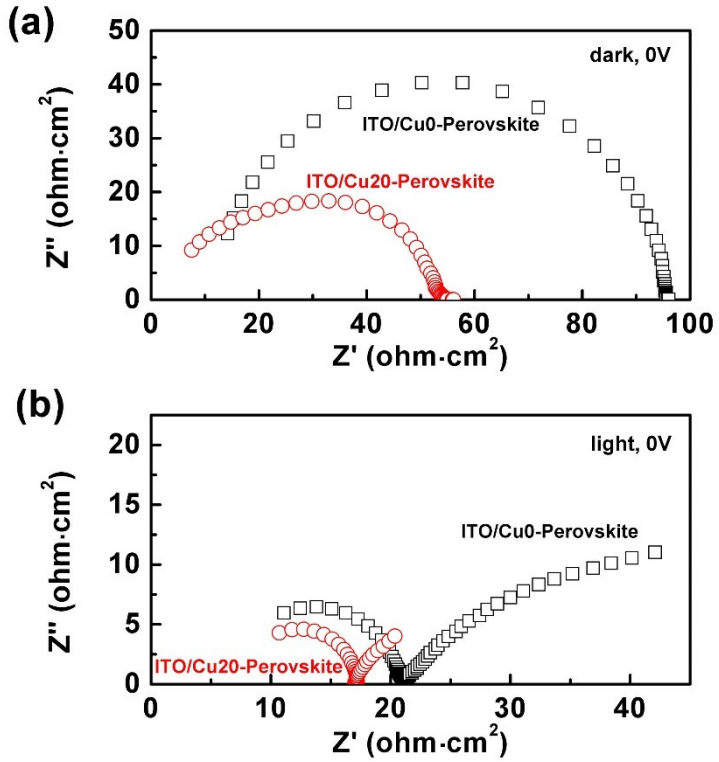

Figure S12. Electrochemical impedance spectra of the undoped and Cu20 doped perovskite films on ITO with Au as counter electrode: a) Niquist plot of the ITO/Cu0-perovskite and ITO/Cu20-perovskite samples measured under dark condition at 0 V (short circuit); b) Niquist plot of the ITO/Cu0-perovskite and ITO/Cu20-perovskite samples measured under AM 1.5 illumination (1 sun) condition at 0 V (short circuit).

The semicircle on ITO/Cu20-perovskite sample was smaller than ITO/Cu0-perovskite sample under dark condition; while there are one arc at higher frequency region and a half-developed semi-cycle at lower frequency region under light condition. The signal measured here corresponded to the charge transfer behavior at the interface and overlapping partially with the charge transport in the cells.[9, 10]

Figure S13.

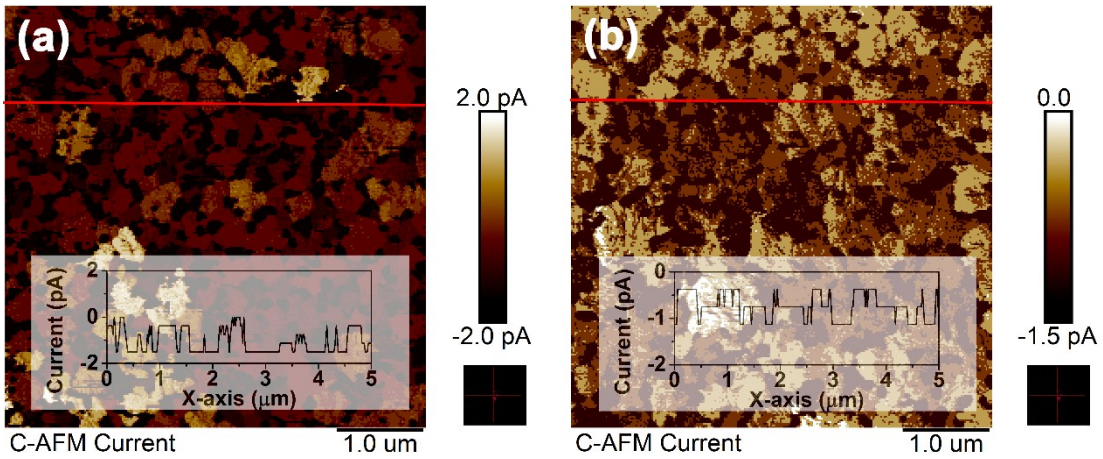

Figure S13. Dark conductive AFM images: a) ITO/perovskite film; b) ITO/Cu-perovskite film. The dark current of the conductive AFM showed a slight lower dark current (~0.7 pA) on the ITO/Cu-perovskite film than ~1 pA on ITO/perovskite film.

Table S4. Parameters of inverted pristine and Cu doped perovskite solar cell devices. [a]

Perovskite solar cells	V_{oc} (V)	J_{sc} (mA/cm^2)	FF (%)	PCE (%)	Average PCE (%)	Champion PCE (%)
Cu free	0.875	16.59	44.54	6.46	6.05±0.64	6.76
Cu10	0.956	21.65	56.81	11.76	11.42±0.45	11.78
Cu20	1.038	22.73	64.54	15.23	15.14±0.67	15.84
Cu30	1.034	22.67	62.02	14.54	14.38±0.79	15.22
Cu40	0.848	20.31	63.58	10.95	10.83±0.87	12.03

[a] the parameters were based on the forward scan.

Figure S14.

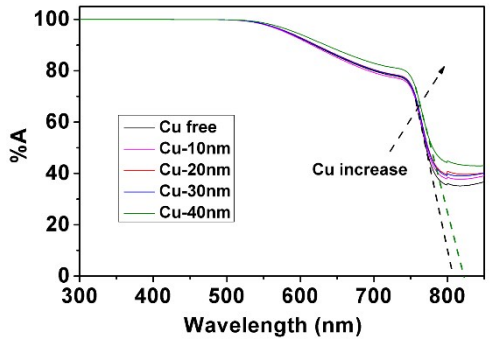

Figure S14. UV-Vis absorption of perovskites. The Cu doping lead to a slight increase of the absorption and a small positive shift of the band absorption edge.

Figure S15

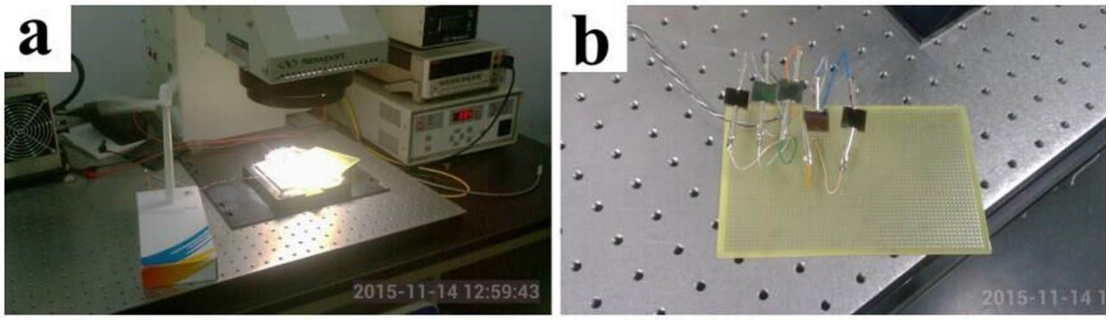

Figure S15. Demonstrating ITO/Cu-perovskite/PCBM/Ag devices in series to power an electric fan: a) stable devices during power out under illumination; b) five devices connected in series. It was shown the devices can power stably the fans under simulated solar light easily under ambient condition, even the devices were not sealed.

Figure S16

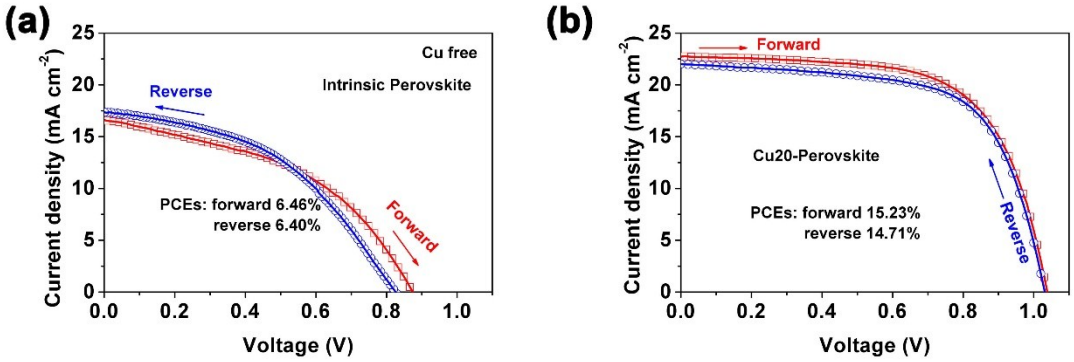

Figure S16. The hysteresis behavior of the perovskite solar cells: a) intrinsic perovskite solar cell; b) Cu20 doped perovskite solar cell. Under ambient condition, the devices showed a larger hysteresis on pristine perovskite on ITO substrate when the potential sweeping forward (from short circuit to open circuit) or reverse. This might be due to the not perfect charge collection as those HTL layers are absent.

Figure S17

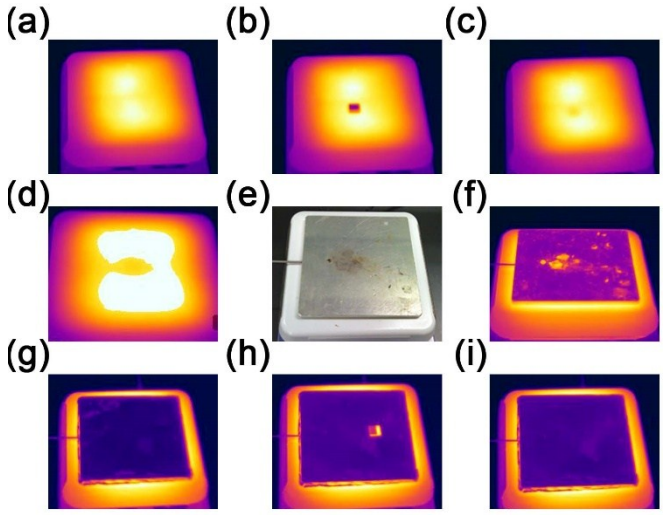

Figure S17. IR thermal images of the hotplate for perovskite film preparation by using a IKA C-MAG HS 7 Digital hotplate and a FLIR T335 camera: a) bare hotplate; b) hotplate with a ITO glass; c) bare hotplate after the ITO glass was removed; d) hotplate with less uniform distribution during the heating; e) digital camera image of additional metal plate on hotplate (horizontal probe is thermal couple); f) contaminated surface of metal plate on hotplate; g) clean surface of metal plate on hotplate; h) clean surface of metal on hotplate with an ITO glass; i) clean surface of metal on hotplate after the ITO glass was removed. The color of the metal plate is lower than the ceramic surface hotplate is due to the less IR emission difference on metal.

References:

1. Y. Shirahata and T. Oku, *AIP Conference Proceedings*, 2017, **1807**, 020008.
2. J. J. Chen and N. Winograd, *Surface Science*, 1995, **326**, 285-300.
3. A. Calloni, A. Abate, G. Bussetti, G. Berti, R. Yivlialin, F. Ciccacci and L. Duò, *J. Phys. Chem. C*, 2015, **119**, 21329-21335.
4. J. H. Yun, I. Lee, T.-S. Kim, M. J. Ko, J. Y. Kim and H. J. Son, *Journal of Materials Chemistry A*, 2015, **3**, 22176-22182.
5. C. Li, S. Tscheuschner, F. Paulus, P. E. Hopkinson, J. Kießling, A. Köhler, Y. Vaynzof and S. Huettner, *Advanced Materials*, 2016, **28**, 2446-2454.
6. G. Sadoughi, D. E. Starr, E. Handick, S. D. Stranks, M. Gorgoi, R. G. Wilks, M. Bär and H. J. Snaith, *ACS Applied Materials & Interfaces*, 2015, **7**, 13440-13444.
7. L. Kronik and Y. Shapira, *Surf. Sci. Rep.*, 1999, **37**, 1-206.
8. P. Atkins and J. d. Paula, *Atkins' Physical Chemistry*, W. H. Freeman and Company, 8th edn., 2005.
9. W. Yan, Y. Li, Y. Li, S. Ye, Z. Liu, S. Wang, Z. Bian and C. Huang, *Nano Energy*, 2015, **16**, 428-437.
10. H. Wei, J. Xiao, Y. Yang, S. Lv, J. Shi, X. Xu, J. Dong, Y. Luo, D. Li and Q. Meng, *Carbon*, 2015, **93**, 861-868.